



OPEN ACCESS

EDITED BY

Zlatko Trajanoski,
Medical University of Innsbruck, Austria

REVIEWED BY

Alexander Kirchmair,
Medical University of Innsbruck, Austria
Stefan Salcher,
Innsbruck Medical University, Austria

*CORRESPONDENCE

Hong Zhu

✉ honglei19830319@126.com

Hui Liu

✉ hliu@njtech.edu.cn

†These authors have contributed equally to this work

RECEIVED 09 May 2024

ACCEPTED 24 September 2024

PUBLISHED 15 October 2024

CITATION

Luo J, Gao Q, Wang M, Liu H and Zhu H (2024) Single-cell and spatial transcriptome characterize coinhibitory cell-cell communications during histological progression of lung adenocarcinoma. *Front. Immunol.* 15:1430163. doi: 10.3389/fimmu.2024.1430163

COPYRIGHT

© 2024 Luo, Gao, Wang, Liu and Zhu. This is an open-access article distributed under the terms of the [Creative Commons Attribution License \(CC BY\)](https://creativecommons.org/licenses/by/4.0/). The use, distribution or reproduction in other forums is permitted, provided the original author(s) and the copyright owner(s) are credited and that the original publication in this journal is cited, in accordance with accepted academic practice. No use, distribution or reproduction is permitted which does not comply with these terms.

Single-cell and spatial transcriptome characterize coinhibitory cell-cell communications during histological progression of lung adenocarcinoma

Judong Luo^{1†}, Qianman Gao^{2†}, Meihua Wang³, Hui Liu^{2*} and Hong Zhu^{1*}

¹Department of Radiotherapy, Tongji Hospital, School of Medicine, Tongji University, Shanghai, China,

²College of Computer and Information Engineering, Nanjing Tech University, Nanjing, Jiangsu, China,

³Department of Pathology, Changzhou Tumor Hospital, Changzhou, Jiangsu, China

Introduction: Lung adenocarcinoma, a prevalent and lethal malignancy globally, is characterized by significant tumor heterogeneity and a complex tumor immune microenvironment during its histologic pattern progression. Understanding the intricate interplay between tumor and immune cells is of paramount importance as it could potentially pave the way for the development of effective therapeutic strategies for lung adenocarcinoma.

Methods: In this study, we run comparative analysis of the single-cell transcriptomic data derived from tumor tissues exhibiting four distinct histologic patterns, lepidic, papillary, acinar and solid, in lung adenocarcinoma. Furthermore, we conducted immunofluorescence assay and spatial transcriptomic sequencing to validated the spatial co-localization of typical co-inhibitory factors.

Results and Discussion: Our analysis unveiled several co-inhibitory receptor-ligand interactions, including PD1-PDL1, PVR-TIGIT and TIGIT-NECTIN2, that potentially exert a pivotal role in recruiting immunosuppressive cells such as M2 macrophages and Tregs into LUAD tumor, thereby establishing immunosuppressive microenvironment and inducing T cells to exhaustion state. Furthermore, The expression level of these co-inhibitory factors, such as NECTIN2 and PVR, were strongly correlated with low immune infiltration, unfavorable patient clinical outcomes and limited efficacy of immunotherapy. We believe this study provides valuable insights into the heterogeneity of molecular, cellular interactions leading to immunosuppressive microenvironment during the histological progression of lung adenocarcinoma. The findings could facilitate the development of novel immunotherapy for lung cancer.

KEYWORDS

histologic pattern, scRNA-seq, cell-cell interactions, immunosuppressive microenvironment, spatial transcriptomics, immunofluorescence assay

Introduction

Lung cancer has the highest incidence among all malignant tumors in men worldwide, causing over a million deaths every year. Lung adenocarcinoma (LUAD) is the predominant histological subtype (1), accounting for 40% of lung cancer patients. The progression and prognosis of LUAD are closely associated with the emergence of morphologically distinct tumor regions, termed histologic patterns (2), including lepidic, papillary, acinar, and solid patterns. These patterns reflect the increasing aggressiveness of the tumor as it progresses. Previous studies have reported that genomic alterations, such as tumor mutational burden (TMB) and copy number variation (CNV), also increased during the histological progression (3–6). However, the tumor heterogeneity and intercellular interactions that contribute to the immunosuppressive tumor microenvironment (TME) during the histological progression remain elusive.

Solid tumors are often characterized by highly complex TME that comprises infiltrating immune cells, stromal cells, chemokines, and extracellular matrix components. Tumor cells dynamically interact with TME to create a low-oxygen, low-pH, pro-inflammatory, and immunosuppressive environment that promotes the progression of cancer and influences patient's response to drug treatment. Single-cell RNA sequencing (scRNA-seq) enables a comprehensive analysis of the cellular diversity and heterogeneity within tumor tissues (7–9). By profiling the gene expression of individual cells, scRNA-seq offers a valuable chance to reveal the intratumoral heterogeneity and cell-cell communication mediated by ligand-receptor interactions (10). For instance, Qi et al. studied the intratumoral heterogeneity in colorectal cancer (CRC) tumors and adjacent tissues, with a particular focus on the interplay between SPP1+ macrophages and FAP+ fibroblasts. The co-localization of these two cell types was substantiated through the use of immunofluorescence staining and spatial transcriptomics (11). Zhang et al. have studied the interaction between malignant cells and regulatory T cells (Tregs) in intrahepatic cholangiocarcinoma (ICC), and found that TIGIT-PVR signal was enriched between Tregs and malignant cells (12). Kim et al. have studied the cell-cell communications in different metastatic tumors of lung adenocarcinoma (13). Nevertheless, there was a dearth of studies exploring the molecular features and intercellular interactions during the histologic pattern progression of lung adenocarcinoma.

In this study, we employed the scRNA-seq data to elucidate molecular heterogeneity, intercellular communications, and immunosuppressive landscapes of lung adenocarcinoma with different histologic patterns. We revealed that the co-inhibitory ligand-receptor interactions were more prevalent and prominent in the solid pattern. Specifically, the tumors with high expression levels of NECTIN2 and PVR exhibited low immune infiltration level, limited response to immunotherapy and poor prognosis. Moreover, our immunofluorescence experiment confirmed the spatial co-localization of cells expressing high levels of PVR and TIGIT molecules in the solid pattern, but not in the lepidic pattern. We further performed spatial transcriptome sequencing to validate the co-localization of these co-inhibitory factors. These findings suggested that tumor cells escaped immune surveillance by

upregulating the expression of NECTIN2 and PVR immune inhibitory molecules to reduce immune cell infiltration. As far as our knowledge, this is the first study that used the single-cell and spatial transcriptomic data to explore the molecular mechanism underlying the histologic pattern progression of LUAD. We believe that our study provided insight into the immunosuppressive microenvironment formation and the underlying mechanism during the lepidic-to-solid progression of lung adenocarcinoma.

Materials and methods

Ethics approval statement

The ethical approval has been obtained from the institutional review board the Affiliated Tongji Hospital of Tongji University, Shanghai, China. Patients gave informed consent at hospitalization.

Single-cell transcriptomic data source

The scRNA-seq data of four histologic patterns was downloaded from a prior study (14), which includes one lepidic sample, one papillary sample, two acinar samples and two solid samples.

Spatial transcriptomics library and sequencing

Two specimens of lung adenocarcinoma, each corresponding to the lepidic and solid histologic patterns as confirmed through histologic scrutiny, were procured in accordance with standard surgical protocols. These specimens underwent a process of formalin fixation and were subsequently encapsulated within paraffin-embedded tissue blocks. The specimens were then sectioned and subjected to hematoxylin and eosin (H&E) staining to facilitate subsequent imaging at a resolution of 40x (equivalent to 0.25 micron/pixel) via the use of Aperio GT450 scanners. The tissue slides were then conveyed to the Genomics core, where following the deconvolving of the tissue, the Visium CytAssist device was employed to transfer transcriptomic probes from the original glass slides to capture areas on Visium slides measuring 11mm x 11mm. Comprehensive transcriptomic profiling was achieved post mRNA permeabilization, through poly(A) capture and probe hybridization. The resultant libraries were sequenced utilizing the Illumina Novaseq 6000, using paired-end sequencing with a read length of 150 base pairs.

Spatial transcriptomics data analysis

Visium spatial transcriptomics profiles for samples contained 18,085 genes across several thousand locations throughout each slide. The profiles were then subjected to filtering process: spots with fewer than 500 genes, genes expressed in fewer than 3 spots, and spots with mitochondrial gene expression exceeding 15% were excluded from

the analysis. Following the removal of regions lacking tissue using a custom annotation tool augmented by the SAM, a total of 4992 spots were obtained from the lepidic sample and 3701 spots from the solid sample. Each Visium spot covers a circular capture area with a diameter of 50-micron (200 pixels) at 40x magnification. Histology images and FASTQ files were processed using the Space Ranger pipeline and sequencing data were aligned to the human reference genome (Ensemble Genome GRCh38). The output generated was imported into Seurat for further analysis, including dimensional reduction, clustering and data integration.

scRNA-seq data quality control and cell type annotation

The scRNA-seq data was processed and analyzed using the Seurat R package. Cells were removed if they had more than 20,000 UMIs, more than 5,000 or fewer than 500 expressed genes, or >30% UMIs that were derived from the mitochondrial genome. The batch effect across different samples was mitigated using Seurat's CCA algorithm. Prior to merging the data, the expression matrix of each sample was standardized using the `NormalizeData` function and the top 2000 variable genes were selected for principal component analysis (PCA) using the `FindVariableFeatures` function. Next, the merged data was normalized using the `ScaleData` function, clustering analysis was performed using the first 30 principal components at resolution 0.8, and visualization was performed using the UMAP algorithm. The classic marker genes used to identify the 13 main cell types were jointly determined by the `FindAllMarkers` function and literature research, and finally the following genes were used to identify different cell types: CD8⁺ T (CD8A, CD8B), CD4⁺ T (IL7R), Tumor cells (EPCAM, KRT19, KRT7), Tregs (FOXP3, IL2RA), Macrophages (CD68, C1QA, C1QC), Plasma cells (IGHG1, JCHAIN, CD79A), B cells (MS4A1, CD19), NK cells (NKG7, GNLY, KLRD1), Monocytes (S100A8, S100A9, FCN1), Fibroblasts (LUM, PDGFRA, ACTA2), Mast cells (TPSAB1, TPSB2, KIT, GATA2), Endothelial cells (VWF, CLDN5, CALCRL), Dendritic cells (CD86, CD1C).

scRNA-seq-based CNV estimation

The `inferCNV` R package was used to infer copy number alterations in various cell types, using the gene expression of B cells as a reference. For parameter setting of `inferCNV`, cutoff was set to 0.1, cluster by groups was set to T. The cell hierarchical clustering method of the ward deviation sum of squares method (`ward.D2`) was used to cluster cells and denoised the results.

Intercellular interaction analysis

CellPhoneDB was used to infer interactions between different cell types. For genes expressed in a cell population, the percentage of

cells expressing the gene and the average gene expression were calculated, and the gene was removed if it was expressed in only 10% or less of the cells in the population. Cell-cell interactions were inferred from the gene expression levels by 1000 permutation tests, and then an adjacency matrix was generated for all cell-cell interactions and displayed on a heat map. The relative expression levels (z-scores) of partial ligands or receptors were visualized using the `ggplot2` (15) package.

Immunofluorescence staining

The immunofluorescence staining was performed to examine the localization of TIGIT, NECTIN2 and PVR in the pathological tissues of patients with two histologic patterns. Paraffin sections of pathological tissues from LUAD patients with both histologic patterns were first deparaffinized and hydrated, followed by antigen retrieval. The primary antibody mixture was added at a ratio of 1:1000: TIGIT (Abcam, Ab243903) + NECTIN2 (Abcam, Ab269721) or TIGIT (Abcam, Ab243903) + PVR (Ab307687), placed in a wet box, and incubated overnight at 4°C; Then added two fluorescent secondary antibodies: Fluorescein (FITC)-conjugated Affinipure Goat Anti-Rabbit IgG(H+L), Proteintech, SA00003-2 + CoraLite594-conjugated Goat Anti-Mouse IgG(H+L), Proteintech, SA00013-3 and Fluorescein (FITC)-conjugated Affinipure Goat Anti-Rabbit IgG(H+L), Proteintech, SA00003-2 + Rhodamine (TRITC)-conjugated Goat Anti-Rat IgG(H+L), Proteintech, SA00007-7, placed in a humid box at room temperature and incubated in the dark for 2 hours; then counterstaining with DAPI and incubated in the dark for 15 minutes, and finally sealed the slides with an anti-fluorescence quencher, and dried them at 37°C for storage.

Trajectory analysis

First, we extracted CD8⁺ T cell subsets for quality control, normalization, and screening of highly variable genes to ensure the reliability of the data. Next, PCA was used to reduce the dimensionality of the high-dimensional gene expression data and extract the first few principal components for subsequent analysis. To further reduce the complexity of the data and identify different cell clusters, we used UMAP to project the reduced-dimensional data. Next, Slingshot was used to infer the differentiation trajectory of CD8⁺ T cells. Slingshot mainly consists of two stages, the inference of the global lineage structure and the inference of pseudo-time variables of cells along each lineage. The first stage uses a cluster-based minimum spanning tree (MST) to stably identify the key elements of the global lineage structure, namely the number of lineages and the location of their branches; the second stage evaluates the potential cell-level pseudo-time changes of each lineage by fitting branch curves. Finally, the identified pathways were mapped to UMAP projections for visualization.

Survival analysis

In this study, the survival analysis were conducted by Kaplan-Meier method, and the log-rank test was used to compare the differences in survival rates between different groups. The survival package was used to perform proportional hazards hypothesis tests and fitted survival regressions. The patients were grouped using the median grouping method and the significance level was set at 0.05. The survminer (16) package was used to plot the Kaplan-Meier survival curves.

Tumor immune microenvironment analysis

The CIBERSORTx tool was used to calculate immune cell infiltration levels using the gene expression matrix, the limma package was used for differential analysis of immune cells, and the vioplot package was used for visualization. The score of the TME was calculated using the ESTIMATE package, and the t-test was used to evaluate statistical significance. $p < 0.05$ is represented by *, $p < 0.01$ is represented by **, and $p < 0.001$ is represented by ***.

Correlation analysis

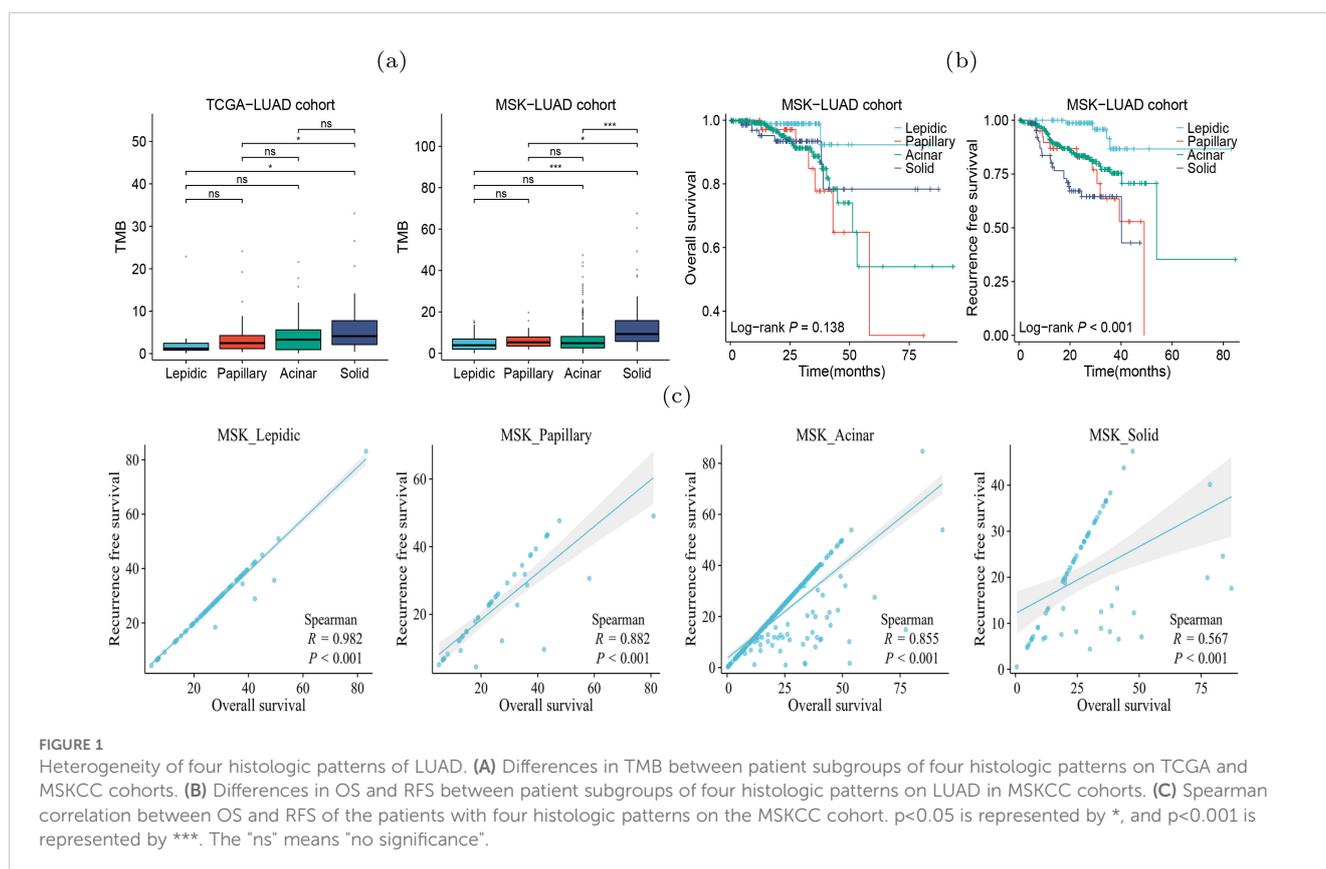
The Spearman correlation between overall survival and recurrence free survival on MSK-IMPACT LUAD cohort was calculated for lepidic and solid patterns, respectively. Spearman

correlation coefficients were also calculated between biomarker genes on TCGA-LUAD cohort. The absolute value of the correlation coefficient represents the degree of correlation: 0-0.3 represents weak or no correlation; 0.3-0.5 represents weak correlation; 0.5-0.8 represents moderate correlation; 0.8-1 represents strong correlation. Specifically, the data with expression values of zero or close to zero in some samples were removed to eliminate the influence of extreme values on analytical results. Also, the samples containing missing values were deleted. The correlation coefficient and p -value were calculated to determine whether the observed correlation was statistically significant. Finally, ggplot2 package was used for visualization.

Results

Different histologic patterns showed molecular heterogeneity and prognosis

Tumor heterogeneity arises from diverse molecular mechanism during tumor progression (17), resulting in substantial differences in the tumor microenvironment (TME), tumor mutation burden (TMB), and clinical outcomes. We explored the TMB differences between the four histologic patterns On the TCGA-LUAD (lepidic: $n=10$; papillary: $n=47$; acinar: $n=65$; solid: $n=58$) and MSK-IMPACT-LUAD (lepidic: $n=88$; papillary: $n=43$; acinar: $n=368$; solid: $n=68$) cohorts, and found that the solid pattern had higher TMB than the other patterns in both cohorts (Figure 1A), indicating a higher



rate of genetic mutations in the solid pattern. Moreover, On the MSK-IMPACTLUAD cohort, we observed significant differences in the survival outcomes between four histologic patterns. Patients with solid pattern had lower relapse-free survival (RFS) than those in other patterns (Figure 1B), indicating higher degree of tumor growth and invasiveness in the solid pattern. Our results are consistent with the findings of previous studies (5, 6). We also found that OS was highly correlated with RFS in patients with lepidic pattern and only weakly correlated in those with solid pattern (Figure 1C). This suggested that the tumor in solid pattern exhibited higher degree of resistance to drug treatment.

scRNA-seq revealed increasing tumor heterogeneity during histologic pattern progression

To further elucidate the molecular heterogeneity of four histologic patterns, we obtained scRNA-seq data of six LUAD samples (one lepidic, one papillary, two acinar and two solid) from a prior study (14). After quality control, 35,107 cells remained for subsequent analysis. We normalized and standardized the data and selected the top 2,000 highly variable genes. Utilizing the Uniform Manifold Approximation and Projection (UMAP) dimensionality reduction, we identified 21 cell clusters (Supplementary Figure S1), comprising 13 cell types (Figure 2A). The mean expression levels of the marker genes of each cell type were shown in Figure 2B. The epithelial cell marker genes EPCAM, KRT19, and KRT7 were used to annotate tumor cells that were further verified copy number variations (18). Accordingly, the tumor cells exhibited higher CNVs than other types of cells (Figure 2C, Supplementary Figure S2). Comparative analysis between histologic patterns revealed that tumor cells in the solid pattern had higher CNVs than those in the other patterns, indicating a close link between histologic pattern progression and genomic instability (Figure 2D). By grouping all cells according to histologic patterns, we revealed the differences in cell composition and heterogeneity in the tumor immune microenvironment (Figure 2E, Supplementary Figure S3). In the solid stage, the infiltration level of immune cells in tumor tissues increased, with macrophages and Tregs cells showing the most significant increase, indicating the emergence of immune inhibitory microenvironment during tumor progression. The differences in immune cell composition among different patients were observed (Figure 2F). In summary, single-cell transcriptome revealed the molecular characteristics and heterogeneity of the tumor microenvironment during histologic pattern progression.

Immunosuppressive genes increasingly expressed during histologic progression

The scRNA-seq data showed a diversity of immune inflammatory cells were recruited to the tumor microenvironment, such as tumor-associated macrophages (TAMs), lymphocytes, and mast cells (Figure 2E). The TAMs, comprising M1 and M2 subtypes,

were the predominant tumor-infiltrating immune cell population (19). M2 macrophages mainly promote tumor growth, invasion, metastasis and immune evasion (20, 21). We investigated the expression of HAVCR2 and LGALS9, typical immune suppressive genes, and CD163, an M2 macrophage marker gene, and found that they were co-expressed in the macrophage clusters (Figure 3A), indicating that the TAMs infiltrating the tumor might be M2 subtype. We used gene expression profiles from the TCGA-LUAD cohort (n=598) and GSE43458 cohort (n=110) to assess the expression correlation of these gene (Figures 3B, C). We observed that HAVCR2 gene expression had a strong correlation with CD163 ($r=0.819$ and 0.823 on two cohorts), and LGALS9 also showed weak correlation ($r=0.292$ and 0.317 on two cohorts). High HAVCR2 expression in TAMs has been shown to exert immune suppressive effect (22, 23), thus we speculated that TAMs in LUAD exerted immune suppression through HAVCR2 gene. Subsequently, we stratified the LUAD patients into high and low subgroups based on the HAVCR2 expression level, and estimated the infiltration level of 22 immune cells using the CIBERSORTx tool (24). We discovered that the M2 macrophage infiltration level in the high group was greater than that in the low group (Figure 3D). Meanwhile, we noticed that the infiltration levels of naive B cells and plasma cells in the high group were low, which would lead to reduced ability to kill tumor cells. We further compared the expression of HAVCR2 gene in four histologic patterns and the expression levels in different cell types. The result showed that HAVCR2 expression was higher in solid pattern than others (Figure 3E), and predominantly expressed in macrophages (Supplementary Figure S9). Meanwhile, the proportion of macrophages in the solid pattern was higher than those in the early histologic pattern (Supplementary Figure S3), indicating that tumor microenvironment evolved to be immune suppressive during the histologic pattern progression.

Cell-cell communication analysis revealed immunosuppressive microenvironment

During the occurrence and progression of malignant tumors, a complex cell-cell interaction network is often established to promote immunosuppressive environment and immune evasion. To study the interplay between tumor cells and other cells, CellPhoneDB (25) was used to explore the immune co-inhibitory interactions in four histologic patterns. The results revealed significant differences in the interactions among various cells between the four histologic patterns (Figure 4A). In the lepidic pattern, tumor cells interacted substantially with macrophages and Tregs, indicating that tumor cells recruited TAMs and Tregs into the tumor at the early stage to create immunosuppressive microenvironment. With the histologic pattern progressed, the interactions between tumor cells and immune cells increased markedly. The tumor cells communicated strongly with CD4⁺ T cells, CD8⁺ T cells, Tregs, macrophages and NK cells (Figure 4B).

In particular, we found that the NECTIN2-TIGIT immune coinhibitory interactions, mediated by the NECTIN2 ligand expressed on tumor cells and the TIGIT receptor expressed on

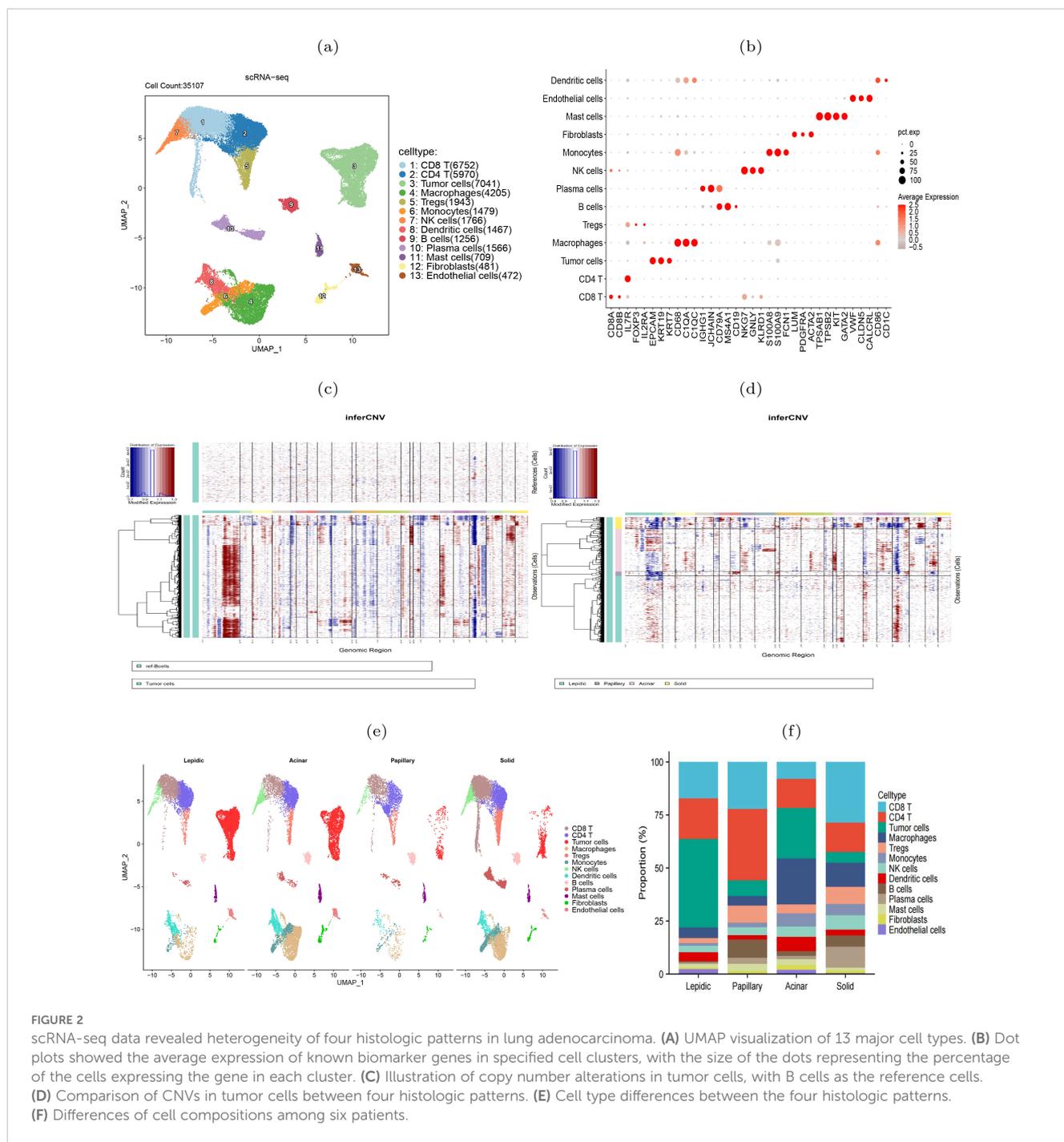


FIGURE 2 scRNA-seq data revealed heterogeneity of four histologic patterns in lung adenocarcinoma. **(A)** UMAP visualization of 13 major cell types. **(B)** Dot plots showed the average expression of known biomarker genes in specified cell clusters, with the size of the dots representing the percentage of the cells expressing the gene in each cluster. **(C)** Illustration of copy number alterations in tumor cells, with B cells as the reference cells. **(D)** Comparison of CNVs in tumor cells between four histologic patterns. **(E)** Cell type differences between the four histologic patterns. **(F)** Differences of cell compositions among six patients.

immune cells, were prevalent during the histologic progression. In the lepidic pattern, the NECTIN2-TIGIT interactions involved tumor cells and NK and Tregs cells, and the interactions extended to encompass tumor cells and CD4⁺ T/CD8⁺ T cells with the histologic pattern progression. This suggested that the tumor cells expressed NECTIN2 to exert co-inhibitory signals and progressively inhibited an increasing number of immune cell types during tumor progression. The gene expression profiles on the TCGA-LUAD cohort corroborated that NECTIN2 was highly expressed in tumor tissues (Supplementary Figure S4). We speculated that the communicative signal between TIGIT and

NECTIN2 represented a crucial mechanism for LUAD tumor cells to establish the immunosuppressive microenvironment. Indeed, several studies have confirmed that the TIGIT-NECTIN2 signal functioned to create immunosuppressive environment in other cancers. For example, Ando et al. also verified that NECTIN2 knockout promoted cell apoptosis and diminished cell proliferation and migration capacity in lung adenocarcinoma via functional assays (26). Ho et al. conducted single-cell sequencing and gene knockout (KO) experiments in mice to verify that the TIGIT-NECTIN2 interaction regulated the immune-suppressive environment and promoted tumor progression in hepatocellular

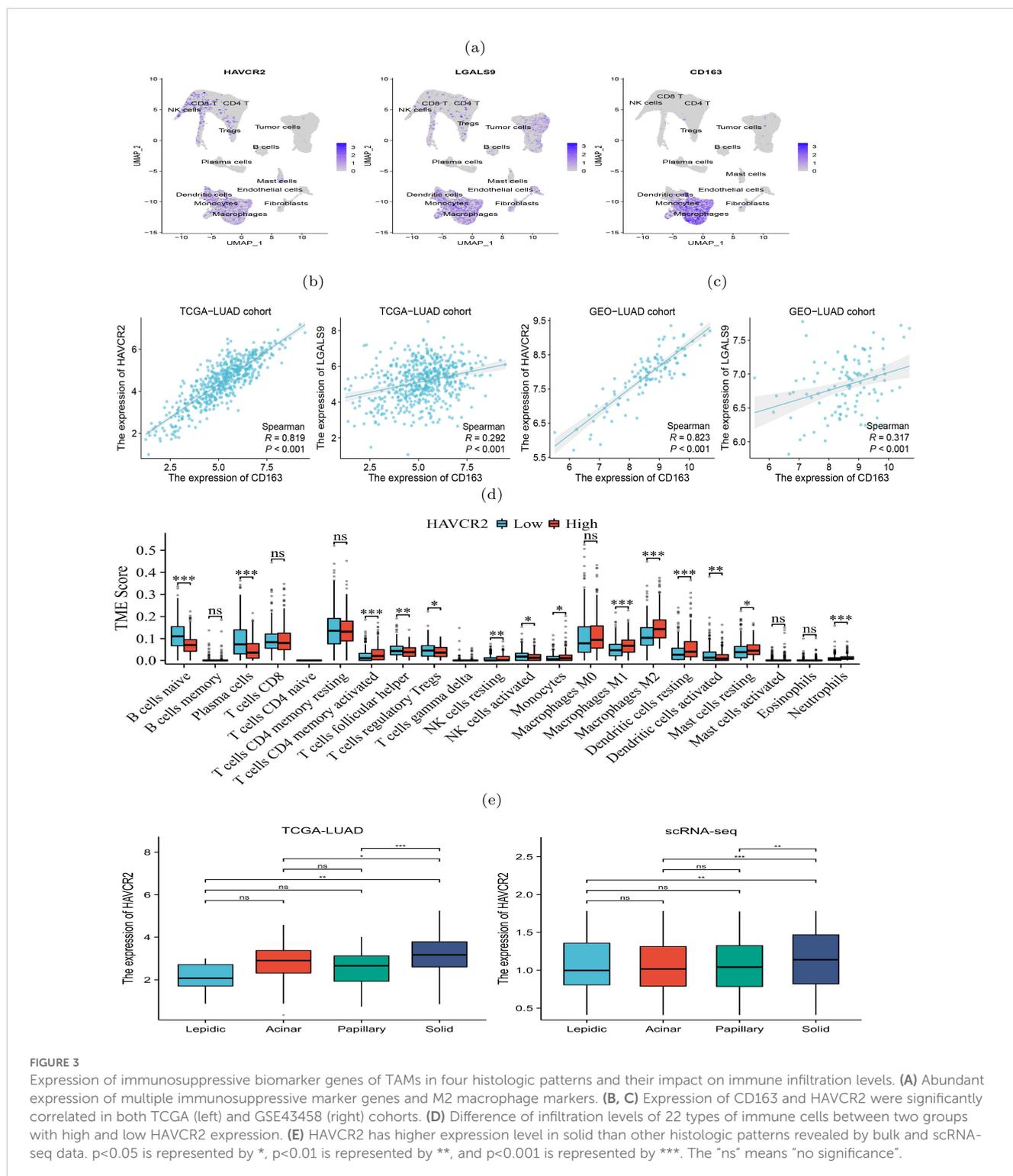


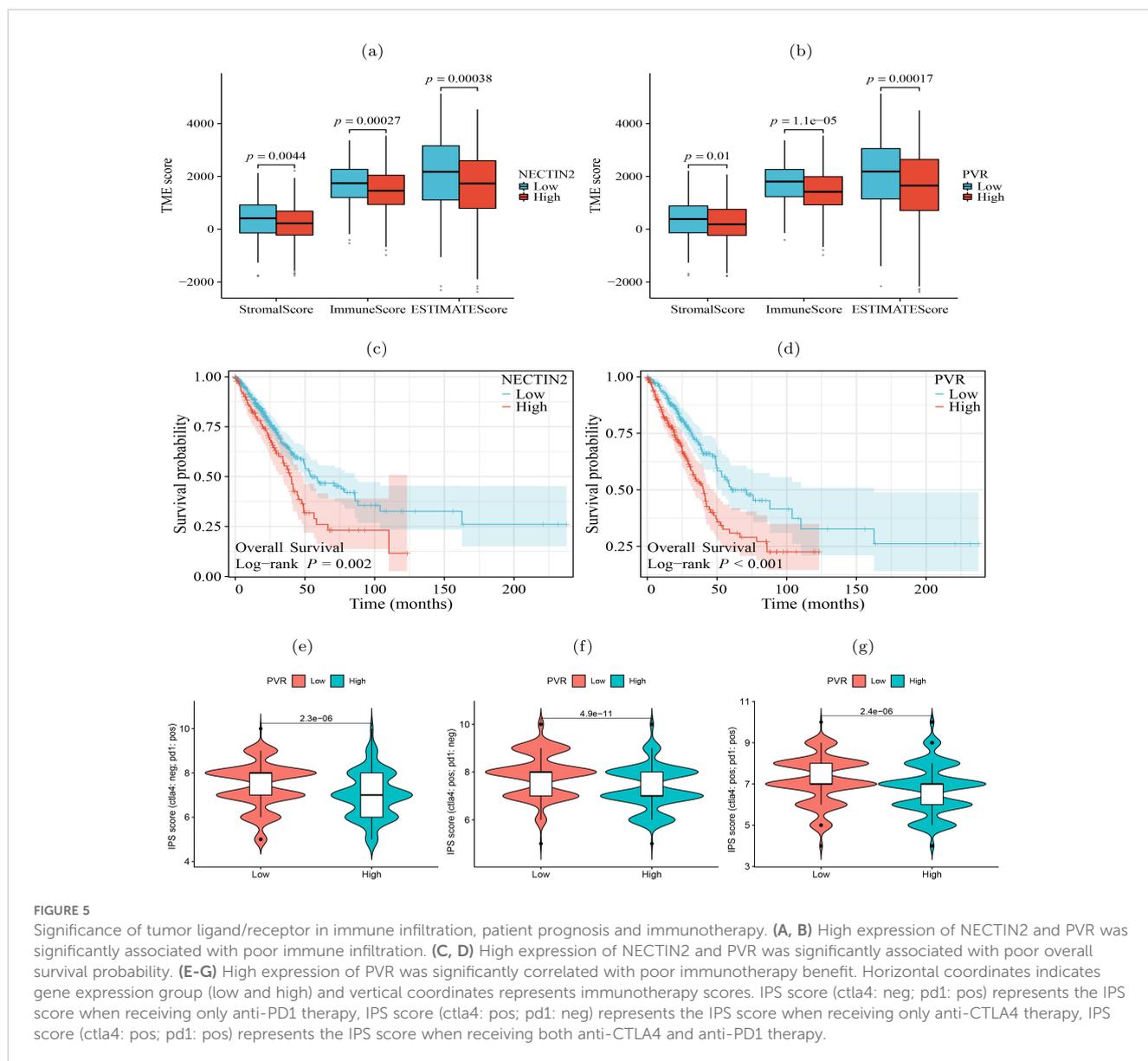
FIGURE 3

Expression of immunosuppressive biomarker genes of TAMs in four histologic patterns and their impact on immune infiltration levels. **(A)** Abundant expression of multiple immunosuppressive marker genes and M2 macrophage markers. **(B, C)** Expression of CD163 and HAVCR2 were significantly correlated in both TCGA (left) and GSE43458 (right) cohorts. **(D)** Difference of infiltration levels of 22 types of immune cells between two groups with high and low HAVCR2 expression. **(E)** HAVCR2 has higher expression level in solid than other histologic patterns revealed by bulk and scRNA-seq data. $p < 0.05$ is represented by *, $p < 0.01$ is represented by **, and $p < 0.001$ is represented by ***. The "ns" means "no significance".

carcinoma (27). Xu et al. showed that the interactions occurred between the metastatic breast cancer cells and TME cells, and their spatial co-localization was verified by immunofluorescence experiments (28).

In contrast to the lepidic pattern, the solid pattern exhibited increased significance of two additional receptor-ligand interactions, PDCD1-CD274 (PD1-PDL1) and PVR-TIGIT, between tumor cells and T cells. It is well-established that the

engagement of immune checkpoint receptors (PD-1) and ligand (PD-L1) is a crucial mechanism by which tumor cells evade immune surveillance (29). TIGIT (T cell immunoglobulin and ITIM domain) is another immune inhibitory receptor protein that has been identified to be a reliably marker of T cell exhaustion (30) and a promising therapeutic target (31–33). PVR is widely expressed in various types of solid tumors (34–37). The immunohistochemistry results from HPA database showed that



findings motivated us to estimate the impact of the expression levels of NECTIN2 and PVR on the tumor microenvironment and prognosis. Running the ESTIMATE tool (39) on bulk RNA-seq data from the TCGA-LUAD cohort, we calculated the level of tumor immune infiltration and found that high expression of NECTIN2 and PVR genes inhibited immune cell infiltration levels (Figures 5A, B). We also assessed the prognostic value of these two genes based on the clinical data of TCGA-LUAD cohort and found that high expression of both genes correlated with poor patient prognosis (Figures 5C, D). Furthermore, we analyzed the IPS immune scores of 512 patients who received anti-PD-1/CTLA-4 immunotherapy in the TCIA database (40) and found that high expression of the PVR gene significantly reduced the immunotherapy response for LUAD patients (Figures 5E-G). Univariate and multivariate Cox regression analysis showed that PVR gene is an independent prognostic factor (Supplementary Figure S6). Also, we conducted Cox regression for other co-

inhibitory genes. The results indicated that only the NECTIN2 gene remains an independent prognostic factor in both univariate and multivariate regression analyses (p -value <0.05 , Supplementary Table S1). These results suggested that overexpression of NECTIN2 and PVR in tumor cells played an important role in the establishment of immune-suppressive environment during LUAD progression.

Immunofluorescence assays and spatial transcriptome validated co-localization of immune coinhibitory ligands and receptors

Our analysis above has revealed that TIGIT-NECTIN2 communication was highly active in four histologic patterns, whereas the PVR-TIGIT communication was only prominent in the papillary and solid patterns. To validate this observation, we

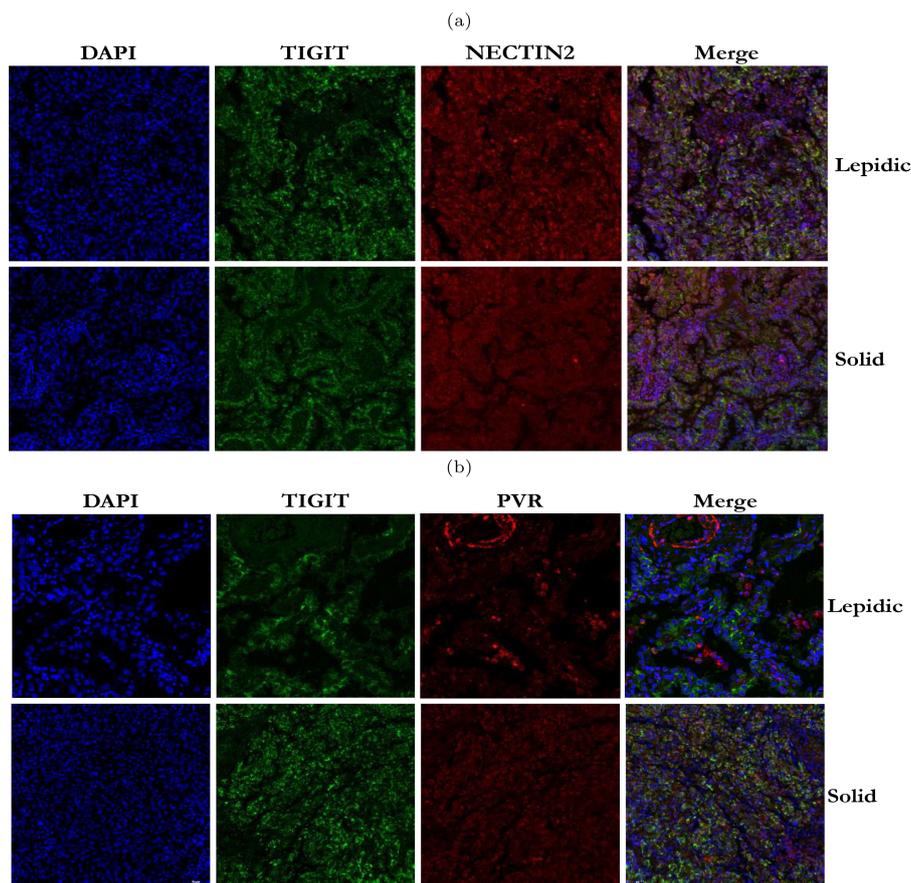


FIGURE 6

Immunofluorescence staining of TIGIT, NECTIN2 and PVR proteins in tumor tissues with two histologic patterns from two patients.

(A) Immunofluorescence image of TIGIT and NECTIN2 proteins in lepidic and solid histologic patterns. (B) Immunofluorescence image of PVR and TIGIT proteins in lepidic and solid histologic patterns. (Scale bar = 50 μ m).

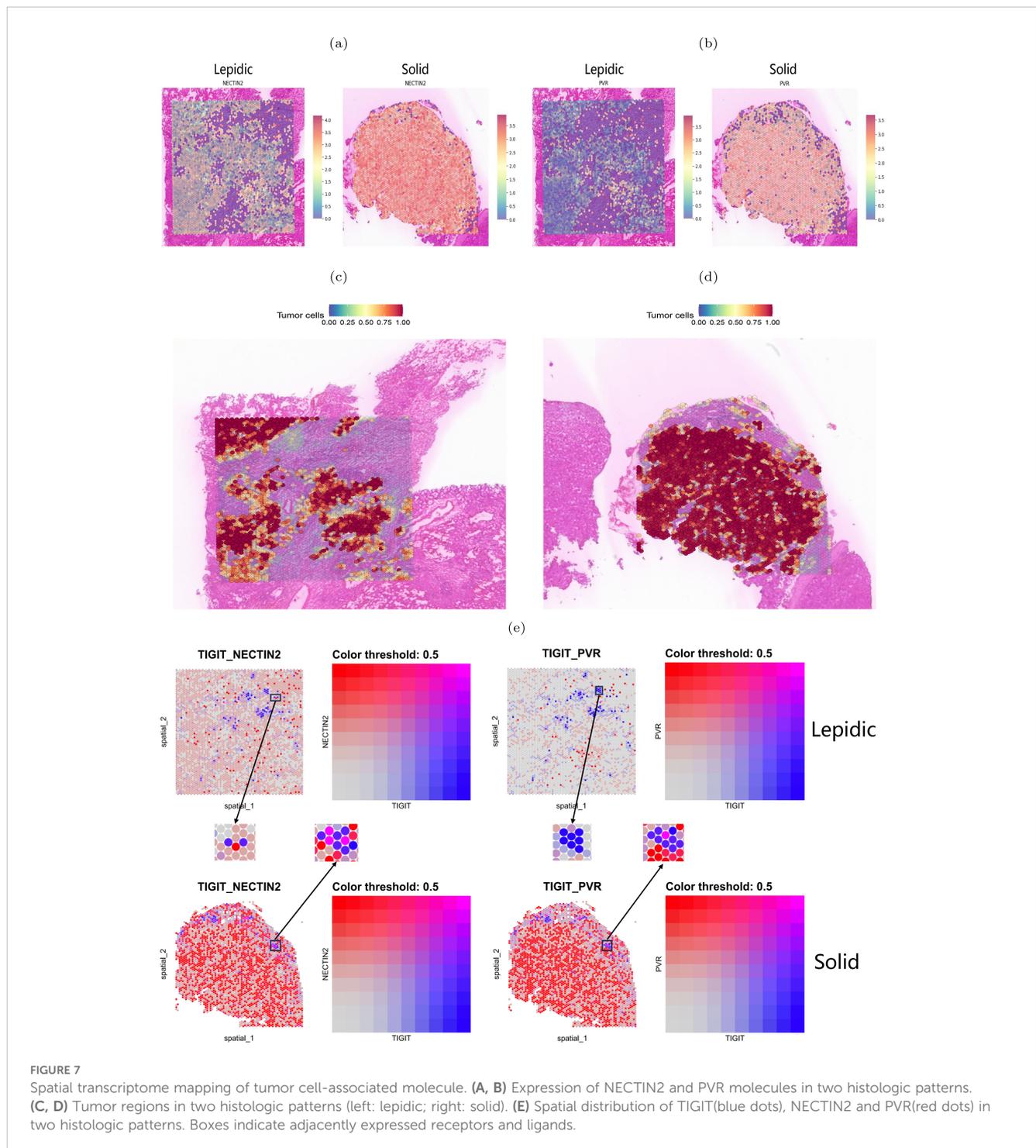
performed immunofluorescence staining on TIGIT, NECTIN2 and PVR proteins on the pathological sections with lepidic and solid patterns. The results showed that TIGIT and NECTIN2 co-localized spatially in both types of tissues (Figure 6A), reflecting that the tumor cells and immune cells communicated frequently through this receptor-ligand axis to create immune-suppressive environment. In contrast, PVR and TIGIT did not exhibit close proximity in lepidic tumor tissue but co-localized spatially in solid tissue (Figure 6B). To further verify the reliability of our findings, we have supplemented the IF staining results from other four patients with lepidic and solid histologic patterns, and the results were still similar to the cell communication analysis results (Supplementary Figure S7). This finding suggested that tumor cells in the solid pattern enhanced immune evasion by expressing more immune co-inhibitory molecules.

We next performed spatial transcriptome sequencing (ST-seq) on two tumor samples with lepidic and solid histologic patterns. As expected, we observed that the solid pattern had higher expression levels of these genes than the lepidic pattern and that they were predominantly localized in the tumor regions (Figures 7A–D). Moreover, we detected spatial co-localization of TIGIT-NECTIN2 in both patterns, while PVR-TIGIT co-localization was more evident in

the solid pattern (Figure 7E). Moreover, we observed that the tumor cell marker gene EPCAM exhibited more similar spatial localization with the NECTIN2 than PVR gene in lepidic pattern, which is consistent with the results of scRNA-seq data. The TIGIT gene demonstrated spatial expression patterns akin to T-cell marker genes CD3D and CD3E in both lepidic and solid patterns (Supplementary Figure S10a). These findings further confirmed that these immune coinhibitory ligand-receptor axes may play a key role in mediating cell-cell communications leading to immunosuppressive microenvironment.

T lymphocytes transitioned to exhaustion during histologic progression

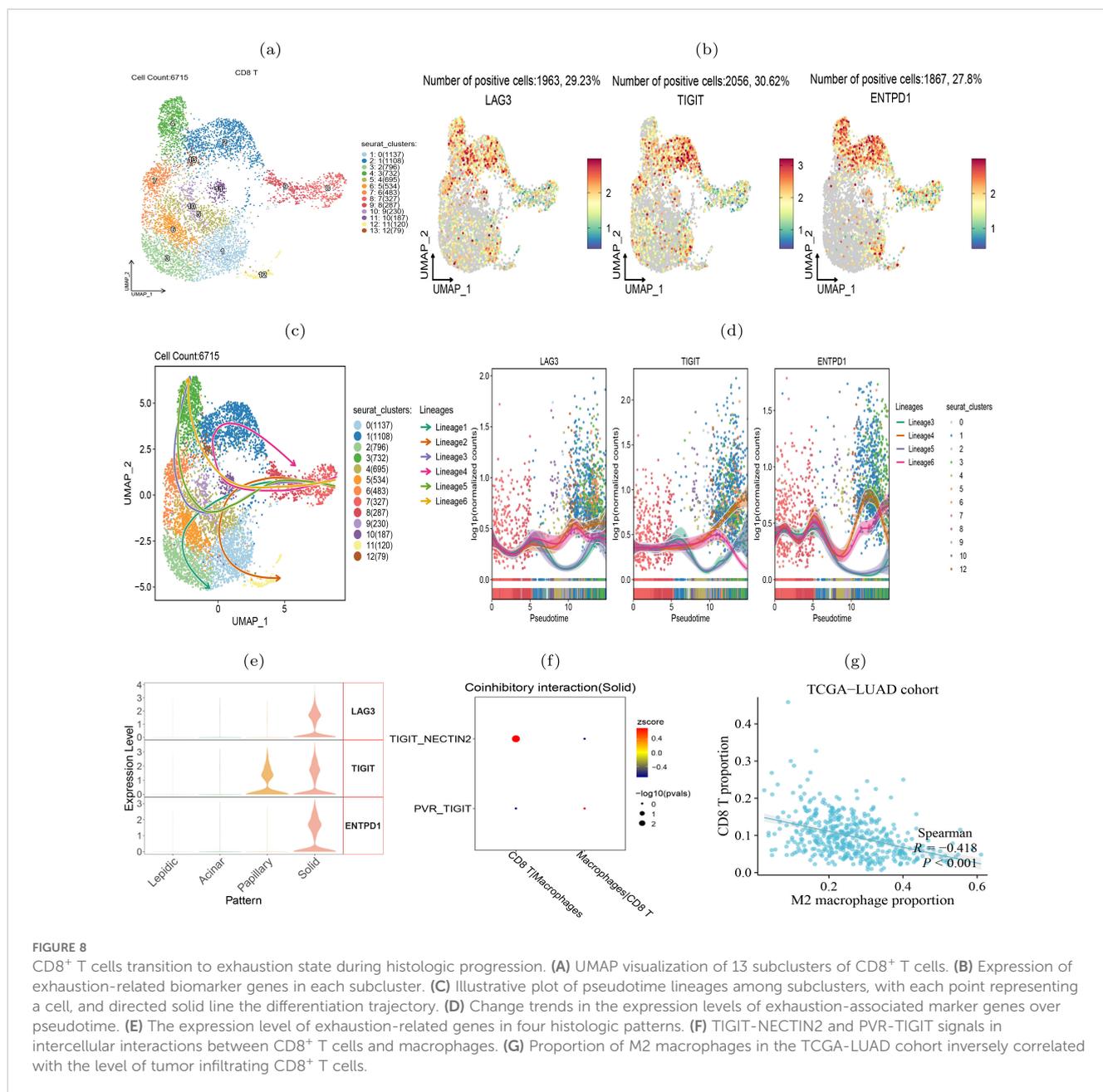
To verify the transition of T cells to exhaustion state during the histologic pattern progression, we clustered the CD8⁺ T cells into 13 subclusters (Figure 8A). We examined the expression of three exhaustion marker genes LAG3, TIGIT and ENTPD1 in each cluster and found that they were highly expressed in clusters 1, 2, 4, and 13 (Figure 8B), indicating that these T cell subclusters underwent exhaustion state transition. To compare the evolutionary trajectory association between the exhausted and



non-exhausted cells, we conducted pseudotime analysis on all CD8⁺ T cells using Slingshot (41) and found that CD8⁺ T cells formed six differentiation lineages, with lineage 3, 4, 5 and 6 showing the transition from non-exhausted state to exhausted state (Figure 8C). We also calculated the expression level changes of the three exhaustion marker genes along different differentiation lineages and found that their expression levels increased with pseudotime in the four exhaustion lineages (Figure 8D). Moreover, we found that the three exhaustion marker genes were highly expressed in the solid pattern but almost absent in the lepidic and acinar patterns

(Figure 8E), indicating the CD8⁺ T cells transitioned to exhausted state in the advanced stage of LUAD.

Our further intercellular communications analysis revealed a pronounced enrichment of the TIGIT-NECTIN2 interaction between the tumor-associated macrophages (TAMs) and CD8⁺ T cells within the solid tumor pattern (Figure 8F). In addition, we visualized the co-inhibitory receptor-ligand interactions between CD8⁺ T cells and other types of immune cells across four histologic patterns (Supplementary Figure S8). The results suggest that co-inhibitory interactions between TAMs and CD8⁺ T cells became



increasing frequent during the tumor progression, indicating that these interactions may be a contributing factor to CD8⁺ T cell exhaustion. Previous study has demonstrated that CD8⁺ T cells interacted with TAMs to initiate the exhaustion program (42). Accordingly, we observed that the abundance of TAMs was predictive of the scarcity of tumor-infiltrating CD8⁺ T cells, as well as reduced T cell killing activity against tumors (Figure 8G). Another study has also confirmed that NECTIN2-TIGIT colocalized significantly more in tumour than in background spots via single-cell and spatial transcriptomics analysis in non-small cell lung cancer (43). In summary, our analysis showed that during the progression of tumors from lepidic to solid pattern, CD8⁺ T cells gradually became exhausted and lost their ability to kill tumor cells.

Discussion and conclusion

In this study, we conducted comparative analysis of the tumor immune microenvironment between four histologic patterns of lung adenocarcinoma. The burden of tumor mutations gradually increases during the histologic progression from the lepidic to solid pattern. This suggested that genome transit to unstable in the later stages of tumor, leading to cellular dysfunction, disordered proliferation and poor differentiation.

The cell-cell communications landscape in the four histologic patterns indicated that as the LUAD tumor progressed, the level of immune cell infiltration increased, while the immune co-inhibitory interactions between tumor cells and immune cells

synchronously intensified. In the solid pattern, there was an increase in tumor-infiltrating immune cells, especially tumor-associated macrophages and T lymphocytes. The high expression levels of exhaustion-related genes in CD8⁺ T cells reflected the immune-suppressive microenvironment in the solid pattern. Studies have reported that macrophages could hinder T cells from infiltrating into lung cancer tissue (44). We also found that the immune-suppressive molecule HAVCR2 was not only enriched in TAMs, but also highly correlated with M2 macrophage marker gene. HAVCR2 high expression promoted the infiltration of M2 macrophages. In fact, the immune-suppressive role of HAVCR2 in hepatocellular carcinoma has been extensively studied (45, 46), but its mechanism of action in lung adenocarcinoma has not been elucidated. Our future work would explore whether HAVCR2 participate in the creation of immune-suppressive environment and anti-T cell infiltration in lung adenocarcinoma.

It was also found significant cell-cell communications between tumor cells and tumor-infiltrating immune cells via the TIGIT-NECTIN2/PVR pairs. The expression of the tumor-associated ligand/receptor genes NECTIN2 and PVR were enriched in lung adenocarcinoma and inhibited immune cell infiltration. They were also highly correlated with poorer overall survival and immunotherapy response in LUAD patients. TIGIT, a known marker gene of T cell exhaustion, is a potential therapeutic target to improve treatment efficacy for LUAD patients, via monotherapy or in combination with other drugs. For example, the phase II CITYSCOKE trial has evaluated the combination of tiragolumab (anti-TIGIT antibody) and atezolizumab (anti-PD-L1 antibody) for the treatment of non-small cell lung cancer and reported promising therapeutic effects (47). Moreover, our immunofluorescence assay and spatial transcriptomic data confirmed the spatial co-localization of TIGIT-NECTIN2/PVR in the solid pattern.

One limitation of this study is the relatively small sample size of scRNA-seq LUAD samples. Despite the availability of numerous datasets in public repositories, most single-cell sequencing data of lung adenocarcinoma lack pathologic pattern information. This limitation significantly hindered us to expand our dataset to include additional scRNA-seq samples regarding the pathological stages, leading to the constrained sample size in this study. We acknowledge that the limited sample size undermines the robustness of our conclusions, leading to decreased statistical power and weak reproducibility. Another limitation of this study is that the tissue samples used for single-cell sequencing, spatial transcriptomics, and immunofluorescence experiments were not derived from the same patient. Tumor heterogeneity can lead to discrepancies in the proportion of specific cell type across different samples exhibiting same histologic pattern, as well as significant differences in gene expression levels. However, such limitation is often challenging to avoid in practice due to the limited availability of cancer tissue material from biopsy samples, making it difficult to meet the requirements for both single-cell and spatial transcriptomics sequencing.

In summary, our integrative analysis of scRNA-seq, bulk RNA-seq and ST-seq data from four histologic patterns of lung adenocarcinoma, we have revealed the tumor heterogeneity and immune-suppressive landscape during histologic pattern progression. These findings may provide unique insights into the treatment for lung adenocarcinoma patients.

Data availability statement

The gene expression profiles, clinical data and mutation data of TCGA-LUAD patients were obtained from <https://portal.gdc.cancer.gov/>. The gene expression profile of GSE43458 cohort was obtained from <https://www.ncbi.nlm.nih.gov/geo/>. The genomic and clinical data of MSK-IMPACT_LUAD cohort were obtained from <https://www.cbioportal.org/>. IPS scores for lung adenocarcinoma patients were obtained from <https://tcia.at/home>. The spatial transcriptome data produced by this study is available at <https://zenodo.org/records/13337961>.

Ethics statement

The ethical approval has been obtained from the institutional review board of the Affiliated Tongji Hospital of Tongji University, Shanghai, China. Patients gave informed consent at hospitalization.

Author contributions

JL: Conceptualization, Writing – review & editing, Validation, Resources. QG: Data curation, Formal analysis, Visualization, Writing – original draft, Conceptualization. MW: Investigation, Writing – review & editing, Resources. HZ: Supervision, Writing – review & editing, Resources. HL: Conceptualization, Data curation, Investigation, Methodology, Supervision, Writing – review & editing, Project administration.

Funding

The author(s) declare that financial support was received for the research, authorship, and/or publication of this article. This work was supported by National Natural Science Foundation of China (No. 62072058, No. 82073339), Natural Science Foundation of Jiangsu Province (No. BK20231271).

Acknowledgments

We are very grateful to MW from the Department of Pathology at Suzhou University Affiliated Changzhou Cancer Hospital for his invaluable suggestions and assistance in our immunofluorescence experiments.

Conflict of interest

The authors declare that the research was conducted in the absence of any commercial or financial relationships that could be construed as a potential conflict of interest.

Publisher's note

All claims expressed in this article are solely those of the authors and do not necessarily represent those of their affiliated

organizations, or those of the publisher, the editors and the reviewers. Any product that may be evaluated in this article, or claim that may be made by its manufacturer, is not guaranteed or endorsed by the publisher.

Supplementary material

The Supplementary Material for this article can be found online at: <https://www.frontiersin.org/articles/10.3389/fimmu.2024.1430163/full#supplementary-material>

References

- Cancer Genome Atlas Research Network. Comprehensive molecular profiling of lung adenocarcinoma. *Nature*. (2014) 511:543. doi: 10.1038/nature13385
- Tavernari D, Battistello E, Dheilly E, Petruzzella AS, Mina M, Sordet-Dessimoz J, et al. Nongenetic evolution drives lung adenocarcinoma spatial heterogeneity and progression/nongenetic evolution of lung adenocarcinoma heterogeneity. *Cancer Discovery*. (2021) 11:1490–507. doi: 10.1158/2159-8290.CD-20-1274
- Izumchenko E, Chang X, Brait M, Fertig E, Kagohara LT, Bedi A, et al. Targeted sequencing reveals clonal genetic changes in the progression of early lung neoplasms and paired circulating dna. *Nat Commun*. (2015) 6:8258. doi: 10.1038/ncomms9258
- Hu X, Fujimoto J, Ying L, Fukuoka J, Ashizawa K, Sun W, et al. Multi-region exome sequencing reveals genomic evolution from preneoplasia to lung adenocarcinoma. *Nat Commun*. (2019) 10:2978. doi: 10.1038/s41467-019-10877-8
- Li F, Wang S, Wang Y, Lv Z, Jin D, Yi H, et al. Multi-omics analysis unravels the underlying mechanisms of poor prognosis and differential therapeutic responses of solid predominant lung adenocarcinoma. *Front Immunol*. (2023) 14:1101649. doi: 10.3389/fimmu.2023.1101649
- Takuwa T, Ishii G, Nagai K, Yoshida J, Nishimura M, Hishida T, et al. Characteristic immunophenotype of solid subtype component in lung adenocarcinoma. *Ann Surg Oncol*. (2012) 19:3943–52. doi: 10.1245/s10434-012-2428-x
- Montoro DT, Haber AL, Biton M, Vinarsky V, Lin B, Birket SE, et al. A revised airway epithelial hierarchy includes cfr-expressing ionocytes. *Nature*. (2018) 560:319–24. doi: 10.1038/s41586-018-0393-7
- Marjanovic ND, Hofree M, Chan JE, Canner D, Wu K, Trakala M, et al. Emergence of a high-plasticity cell state during lung cancer evolution. *Cancer Cell*. (2020) 38:229–46. doi: 10.1016/j.ccell.2020.06.012
- Dost AF, Moye AL, Vedaie M, Tran LM, Fung E, Heinze D, et al. Organoids model transcriptional hallmarks of oncogenic kras activation in lung epithelial progenitor cells. *Cell Stem Cell*. (2020) 27:663–78. doi: 10.1016/j.stem.2020.07.022
- Baslan T, Hicks J. Unravelling biology and shifting paradigms in cancer with single-cell sequencing. *Nat Rev Cancer*. (2017) 17:557–569. doi: 10.1038/nrc.2017.58
- Qi J, Sun H, Zhang Y, Wang Z, Xun Z, Li Z, et al. Single-cell and spatial analysis reveal interaction of fap+ fibroblasts and spp1+ macrophages in colorectal cancer. *Nat Commun*. (2022) 13:1742. doi: 10.1038/s41467-022-29366-6
- Zhang M, Yang H, Wan L, Wang Z, Wang H, Ge C, et al. Single-cell transcriptomic architecture and intercellular crosstalk of human intrahepatic cholangiocarcinoma. *J Hepatol*. (2020) 73:1118–30. doi: 10.1016/j.jhep.2020.05.039
- Kim N, Kim HK, Lee K, Hong Y, Cho JH, Choi JW, et al. Single-cell rna sequencing demonstrates the molecular and cellular reprogramming of metastatic lung adenocarcinoma. *Nat Commun*. (2020) 11:2285. doi: 10.1038/s41467-020-16164-1
- Bischoff P, Trinks A, Obermayer B, Pett JP, Wiederspahn J, Uhlitz F, et al. Single-cell rna sequencing reveals distinct tumor microenvironmental patterns in lung adenocarcinoma. *Oncogene*. (2021) 40:6748–58. doi: 10.1038/s41388-021-02054-3
- Wickham H. *ggplot2*. Wiley interdisciplinary reviews: computational statistics (State of New Jersey: Wiley Online Library), Vol. 3. (2011). pp. 180–5.
- Kassambara A, Kosinski M, Biecek P, Fabian S. *survminer: Drawing survival curves using 'ggplot2'*. R package version 0.3, Vol. 1. (2017). doi: 10.32614/CRAN.package.survminer
- Vitale I, Shema E, Loi S, Galluzzi L. Intratumoral heterogeneity in cancer progression and response to immunotherapy. *Nat Med*. (2021) 27:212–24. doi: 10.1038/s41591-021-01233-9
- Patel AP, Tirosh I, Trombetta JJ, Shalek AK, Gillespie SM, Wakimoto H, et al. Single-cell rna-seq highlights intratumoral heterogeneity in primary glioblastoma. *Science*. (2014) 344:1396–401. doi: 10.1126/science.1254257
- Dehne N, Mora J, Namgaladze D, Weigert A, Brune B. Cancer cell and macrophage cross-talk in the tumor microenvironment. *Curr Opin Pharmacol*. (2017) 35:12–9. doi: 10.1016/j.coph.2017.04.007
- Chen Y, Song Y, Du W, Gong L, Chang H, Zou Z. Tumor-associated macrophages: an accomplice in solid tumor progression. *J Biomed Sci*. (2019) 26:1–13. doi: 10.1186/s12929-019-0568-z
- Mantovani A, Sozzani S, Locati M, Allavena P, Sica A. Macrophage polarization: tumor-associated macrophages as a paradigm for polarized m2 mononuclear phagocytes. *Trends Immunol*. (2002) 23:549–55. doi: 10.1016/S1471-4906(02)02302-5
- Yan W, Liu X, Ma H, Zhang H, Song X, Gao L, et al. Tim-3 fosters hcc development by enhancing tgf- β -mediated alternative activation of macrophages. *Gut*. (2015) 64:1593–604. doi: 10.1136/gutjnl-2014-307671
- Li H, Wu K, Tao K, Chen L, Zheng Q, Lu X, et al. Tim-3/galectin-9 signaling pathway mediates t-cell dysfunction and predicts poor prognosis in patients with hepatitis b virus-associated hepatocellular carcinoma. *Hepatology*. (2012) 56:1342–51. doi: 10.1002/hep.v56.4
- Newman AM, Liu CL, Green MR, Gentles AJ, Feng W, Xu Y, et al. Robust enumeration of cell subsets from tissue expression profiles. *Nat Methods*. (2015) 12:453–7. doi: 10.1038/nmeth.3337
- Efremova M, Vento-Tormo M, Teichmann SA, Vento-Tormo R. Cellphonedb: inferring cell–cell communication from combined expression of multi-subunit ligand–receptor complexes. *Nat Protoc*. (2020) 15:1484–506. doi: 10.1038/s41596-020-0292-x
- Ando T, Ka M, Sugiura Y, Tokunaga M, Nakagawa N, Iida T, et al. Nectin2 is a prognostic biomarker and potential therapeutic target in lung adenocarcinoma. *Respir Invest*. (2024) 62:582–8. doi: 10.1016/j.resinv.2024.04.002
- Ho DW-H, Tsui YM, Chan LK, Sze KMF, Zhang X, Cheu JWS, et al. Single-cell rna sequencing shows the immunosuppressive landscape and tumor heterogeneity of hbv-associated hepatocellular carcinoma. *Nat Commun*. (2021) 12:3684. doi: 10.1038/s41467-021-24010-1
- Xu K, Wang R, Xie H, Hu L, Wang C, Xu J, et al. Single-cell rna sequencing reveals cell heterogeneity and transcriptome profile of breast cancer lymph node metastasis. *Oncogenesis*. (2021) 10:66. doi: 10.1038/s41389-021-00355-6
- Greenwald RJ, Freeman GJ, Sharpe AH. The b7 family revisited. *Annu Rev Immunol*. (2005) 23:515–48. doi: 10.1146/annurev.immunol.23.021704.115611
- Ostroumov D, Duong S, Wingerath J, Woller N, Manns MP, Timrott K, et al. Transcriptome profiling identifies tigit as a marker of t-cell exhaustion in liver cancer. *Hepatology*. (2021) 73:1399–418. doi: 10.1002/hep.31466
- Dougall WC, Kurtulus S, Smyth MJ, Anderson AC. Tigit and cd 96: new checkpoint receptor targets for cancer immunotherapy. *Immunol Rev*. (2017) 276:112–20. doi: 10.1111/imr.12518
- Stamm H, Oliveira-Ferrer L, Grossjohann EM, Muschhammer J, Thaden V, Brauneck F, et al. Targeting the tigit-pvr immune checkpoint axis as novel therapeutic option in breast cancer. *Oncimmunology*. (2019) 8:e1674605. doi: 10.1080/2162402X.2019.1674605
- Stamm H, Wellbrock J, Fiedler W. Interaction of pvr/pvrl2 with tigit/dnam-1 as a novel immune checkpoint axis and therapeutic target in cancer. *Mamm Genome*. (2018) 29:694–702. doi: 10.1007/s00335-018-9770-7
- Zheng Q, Wang B, Gao J, Xin N, Wang W, Song X, et al. Cd 155 knockdown promotes apoptosis via akt/bcl-2/bax in colon cancer cells. *J Cell Mol Med*. (2018) 22:131–40. doi: 10.1111/jcmm.13301
- Wu L, Mao L, Liu JF, Chen L, Yu GT, Yang LL, et al. Blockade of tigit/cd155 signaling reverses t-cell exhaustion and enhances antitumor capability in head and neck squamous cell carcinoma blockade of tigit/cd155 signaling in hnscc. *Cancer Immunol Res*. (2019) 7:1700–13. doi: 10.1158/2326-6066.CIR-18-0725
- Inozume T, Yaguchi T, Furuta J, Harada K, Kawakami Y, Shimada S. Melanoma cells control antimelanoma ctl responses via interaction between tigit and cd155 in the effector phase. *J Invest Dermatol*. (2016) 136:255–63. doi: 10.1038/JID.2015.404

37. He W, Zhang H, Han F, Chen X, Lin R, Wang W, et al. Cd155/tigit signaling regulates cd8+ t-cell metabolism and promotes tumor progression in human gastric cancer. *Cancer Res.* (2017) 77:6375–88. doi: 10.1158/0008-5472.CAN-17-0381
38. Stengel KF, Harden-Bowles K, Yu X, Rouge L, Yin J, Comps-Agrar L, et al. Structure of tigit immunoreceptor bound to poliovirus receptor reveals a cell–cell adhesion and signaling mechanism that requires cis-trans receptor clustering. *Proc Natl Acad Sci.* (2012) 109:5399–404. doi: 10.1073/pnas.1120606109
39. Duan N. Smearing estimate: a nonparametric retransformation method. *J Am Stat Assoc.* (1983) 78:605–10. doi: 10.1080/01621459.1983.10478017
40. Charoentong P, Finotello F, Angelova M, Mayer C, Efremova M, Rieder D, et al. Pan-cancer immunogenomic analyses reveal genotype-immunophenotype relationships and predictors of response to checkpoint blockade. *Cell Rep.* (2017) 18:248–62. doi: 10.1016/j.celrep.2016.12.019
41. Street K, Risso D, Fletcher RB, Das D, Ngai J, Yosef N, et al. Slingshot: cell lineage and pseudotime inference for single-cell transcriptomics. *BMC Genomics.* (2018) 19:1–16. doi: 10.1186/s12864-018-4772-0
42. Kersten K, Hu KH, Combes AJ, Samad B, Harwin T, Ray A, et al. Spatiotemporal co-dependency between macrophages and exhausted cd8+ t cells in cancer. *Cancer Cell.* (2022) 40:624–38. doi: 10.1016/j.ccell.2022.05.004
43. De Zuani M, Xue H, Park JS, Dentre SC, Seferbekova Z, Tessier J, et al. Single-cell and spatial transcriptomics analysis of non-small cell lung cancer. *Nat Commun.* (2024) 15:4388. doi: 10.1038/s41467-024-48700-8
44. Peranzoni E, Lemoine J, Vimeux L, Feuillet V, Barrin S, Kantari-Mimoun C, et al. Macrophages impede cd8 t cells from reaching tumor cells and limit the efficacy of anti-pd-1 treatment. *Proc Natl Acad Sci.* (2018) 115:E4041–50. doi: 10.1073/pnas.1720948115
45. Kim H-D, Song GW, Park S, Jung MK, Kim MH, Kang HJ, et al. association between expression level of pd1 by tumor-infiltrating cd8+ t cells and features of hepatocellular carcinoma. *Gastroenterology.* (2018) 155:1936–50. doi: 10.1053/j.gastro.2018.08.030
46. Tan S, Xu Y, Wang Z, Wang T, Du X, Song X, et al. Tim-3 hampers tumor surveillance of liver-resident and conventional nk cells by disrupting pi3k signaling. tim-3 hampers the function of tumoral lrnk and cnk cells. *Cancer Res.* (2020) 80:1130–42. doi: 10.1158/0008-5472.CAN-19-2332
47. Rodriguez-Abreu D, Johnson ML, Hussein MA, Cobo M, Patel AJ, Secen NM, et al. CITYSCAPE: primary analysis of a randomized, double-blind, phase II study of the anti-TIGIT antibody tiragolumab plus atezolizumab versus placebo plus atezolizumab as 1L treatment in patients with PD-L1-selected NSCLC. *J Clin Oncol* (2020) 38:9503. doi: 10.1200/JCO.2020.38.15_suppl.9503